Supporting Material for:

A unique isotopic fingerprint of sulfate-driven anaerobic oxidation of methane

Antler, Gilad*, Turchyn, Alexandra V., Herut, Barak, Sivan, Orit

Materials and methods

The new pore fluid data comes from the Southeastern Mediterranean shelf (Site PC6- location: 32° 17.113,N 034° 44.620,E, water depth: 45m—Fig. DR.1 - See supporting online material for analytical methods): The sediment was sampled using a 6m long piston corer and sliced onboard. For methane measurements, ~2 ml of the sediment were taken immediately after slicing, using an edge cut syringe, inserted into a flushed argon bottle containing 5 ml sodium hydroxide (1.5 N), which was then sealed with a crimper. Pore fluids were extracted using a centrifuge flushed with nitrogen. Pore fluid sulfate was precipitated as barium sulfate (barite) using a saturated barium chloride solution. The barite was then washed with 6N HCl and distilled water. For the dissolved inorganic carbon (DIC) and $\delta^{13}C_{DIC}$ measurements the sample was filtered (0.45 μm) and transferred into a syringe. Based on the geochemical pore fluid concentrations, this site shows a distinct sulfate-methane transition zone at a depth of 3.6 m (Fig. DR.2). In addition, the ratio between the depletion of sulfate and the dissolved inorganic carbon, as well as the change in calcium, magnesium and strontium at this site pore water, is -1.1 (Fig. DR.3). This stoichiometry indicates that diffusion-limited sulfate-driven AOM is the dominant process that occurs at this site (e.g. Martens and Berner, 1974; Reeburgh, 1976; Burdige and Komada, 2011).

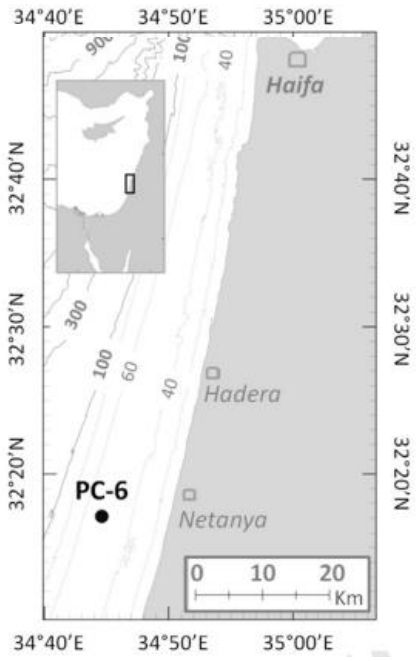

Figure DR.1: Map of the study area in a map of the Eastern Mediterranean region. The dot and indicates the site location.

Analytical methods

Sulfate, calcium and magnesium concentrations were measured by inductivity coupled plasma-atomic emission (ICP-AES, P-E optima 3300) with a precision of 2%. DIC concentrations were measured according to the peak height and calibration curve on the Gas Source Isotopic Ratio Mass Spectrometer (GS-IRMS, Thermo) with an error of 0.2 mM. 1 ml headspace sample was taken from the crimped vial with a gas-tight pressure lock after the bottle was shaken vigorously. Methane was measured from the headspace on a Focus Gas Chromatograph (Thermo) with ShinCarbon column with precision of 2 μM L^{-1}.

$\delta^{13}C_{DIC}$ was measured by a Gas Source Isotopic Ratio Mass Spectrometer (GS-IRMS Thermo, at Ben Gurion University) through a Gas Bench II (GBII) interface. with an error of 0.1‰. The values are reported versus the Vienna Pee Dee Belemnite (VPDB) standard.

For $\delta^{18}O_{SO4}$ analysis, barite was pyrolyzed at 1450°C in a Temperature Conversion Element Analyzer (TC/EA). The resulting carbon monoxide (CO) was measured by continuous helium flow on a GS-IRMS (Thermo Finnegan Delta V Plus, at the Godwin Laboratory, University of Cambridge). For the $\delta^{34}S_{SO4}$ analysis, the barite was combusted at 1030°C in a Flash Element Analyzer (EA), and the resulting sulfur dioxide (SO_2) was measured by continuous helium flow on a GS-IRMS (Thermo Finnegan Delta V Plus Godwin Laboratory, University of Cambridge). Samples for $\delta^{18}O_{SO4}$ ran in replicates (n=3-5) and the standard deviation of these replicate analyses was used as the error (~0.3‰ 1σ). The error for $\delta^{34}S_{SO4}$ was determined using the standard deviation of the standard NBS 127 at the beginning and the end of each run (~0.3‰ 1σ). Samples for both $\delta^{18}O_{SO4}$ and $\delta^{34}S_{SO4}$ were corrected to NBS 127 ($\delta^{18}O_{SO4}$ of 8.6‰ and $\delta^{34}S_{SO4}$ of 20.3‰). The $\delta^{34}S_{SO4}$ values are reported versus Vienna Canyon Diablo Troilite (VCDT) and $\delta^{18}O_{SO4}$ versus Vienna Standard Mean Ocean water (VSMOW).

Results

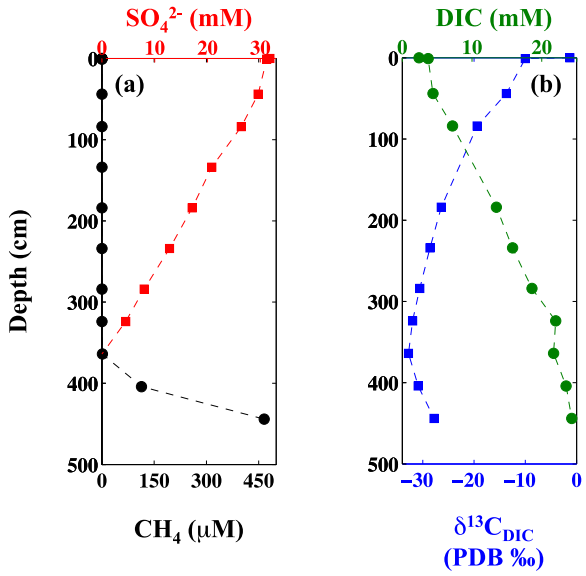

Figure DR.2: Pore fluid profiles of SO_4^{2-} and CH_4 (a), DIC and $\delta^{13}C_{DIC}$ (b). The results demonstrate distinct sulfate-methane transition zone at depth of 3.6m.

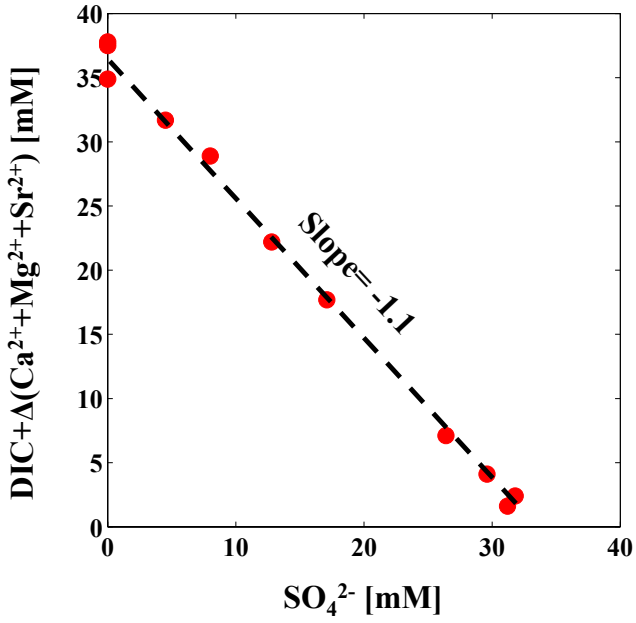

Figure DR.3: Dissolved inorganic carbon (DIC) plus the change in calcium and magnesium concentrations vs. sulfate concentrations. The dashed line is the best-fit linear regression with a slope of -1.1. This stoichiometry indicates that sulfate-driven AOM is the dominant process that consumes sulfate at this location.

Table DR1: Pore fluid analyses at site PC-6

Depth [cm]	SO_4 [mM]	CH_4 [µM]	$\delta^{13}C_{DIC}$	DIC [mM]	$\delta^{18}O_{SO4}$	$\delta^{34}S_{SO4}$
0	31.8		-1.3	2.4	9.4	20.2
1	31.2	0	-10.0	3.7	10.9	21.4
44	29.6	0	-13.7	4.4		
84	26.4	0	-19.4	7.2	12.6	22.5
134	20.8	0			15.2	
184	17.1	0	-26.4	13.5	18.3	25.5
234	12.8	0	-28.6	15.8	20.5	28.2
284	8.0	0	-30.6	18.6	24.0	32.2
324	4.5	0	-32.0	22.0	25.2	34.0
364	0.0	1	-32.8	21.7		
404	0.0	114	-30.9	23.5		
444	0.0	466	-27.8	24.3		

A sensitivity analysis for oxygen and sulfur isotopes in sulfate during sulfate-driven AOM

This calculation was initially performed in Antler et al. (2013) and we only outline the relevant details here. In order to understand the relative evolution of sulfur and oxygen isotopes in sulfate during sulfate-driven AOM, we derive a basic numerical model based on the enzymatic model proposed by Milucka et al. (2012). In the Milucka et al. (2012) enzymatic model, methane oxidation and sulfate reduction to elemental sulfur (or all the way to sulfide) is performed by methanotrophic archaea alone (ANME). Zero-valent sulfur then reacts with sulfide to form disulphide, which subsequently disproportionates into sulfate and sulfide. For each eight sulfate molecules that are brought into the cell, one recycles back to sulfate during this disulfide disproportionation and the other seven molecules are reduced to sulfide.

Some of the specifics of this enzymatic model remain enigmatic which presents challenges for our numerical model. For example both sulfur and oxygen isotopes are partitioned during the various enzymatic steps with unknown kinetic and equilibrium fractionation factors. Here, we perform a carful sensitivity analysis, in order to deal with this uncertainty.

The assumptions in our model include (Fig. S4):

1) The kinetic isotope fractionation between sulfate and zero-valent sulfur is 25±10 ‰ (Rees, 1973)

2) The kinetic oxygen isotopic fractionation is equal to 25% of the sulfur isotopic fractionation between sulfate and zero-valent sulfur (Mizutani, Y. and Rafter 1969).
3) The kinetic isotope fractionation between zero-valent sulfur and sulfide is 25±10 ‰ (Rees, 1973).
4) The isotopic composition of the disulfide was taken as the average value between zero-valent sulfur and sulfide. This is since each one of them contributes the same number of sulfur atoms to the resulting disulfide.
5) The sulfur isotopic fractionation between disulfide and sulfate is 15±15 ‰ (Böttcher et al., 2001).
6) The sulfur isotopic fractionation between disulfide and sulfide is -5±5 ‰ (Böttcher et al., 2001).
7) The result $\delta^{18}O_{SO4}$ during disulfide disproportionation is 20±5 ‰ (Böttcher et al., 2001).

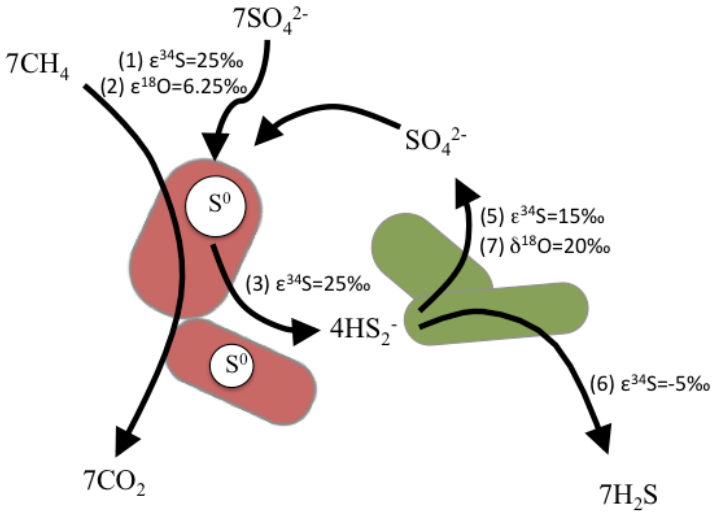

Figure DR.4: Sulfur pathway during sulfate-driven AOM (After Milucka et al., 2012) and the isotopic fractionation associated with each of the steps.

Figure DR.5 summaries all the possible solution for $\delta^{18}O_{SO4}$ vs. $\delta^{34}S_{SO4}$ within the uncertainties of our assumptions. The result for the model suggests that even with these unknowns, all the solutions have a near linear relationship with a slope that varies between 0.24 and 0.4. If we consider only our primary values, Our model suggests that over 40% of the sulfate entering the cell being reoxidized will impact the slope to the point where $\delta^{18}O_{SO4}$ vs. $\delta^{34}S_{SO4}$ slopes higher than 0.4 (Fig. DR.6).

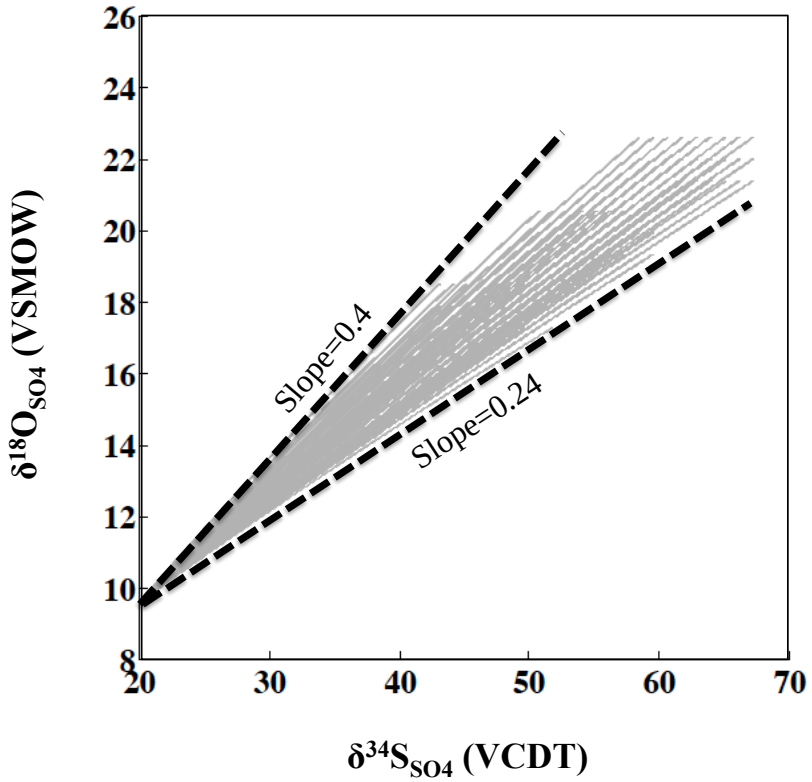

Figure DR.5: The $\delta^{18}O_{SO4}$ vs. $\delta^{34}S_{SO4}$ results from the proposed model. Each of the grey lines represent a solution based on the different combination of the isotope fractionation of sulfur and oxygen isotopes at each step. Dashed lines are the envelope of all the possible solutions within the proposed uncertainty.

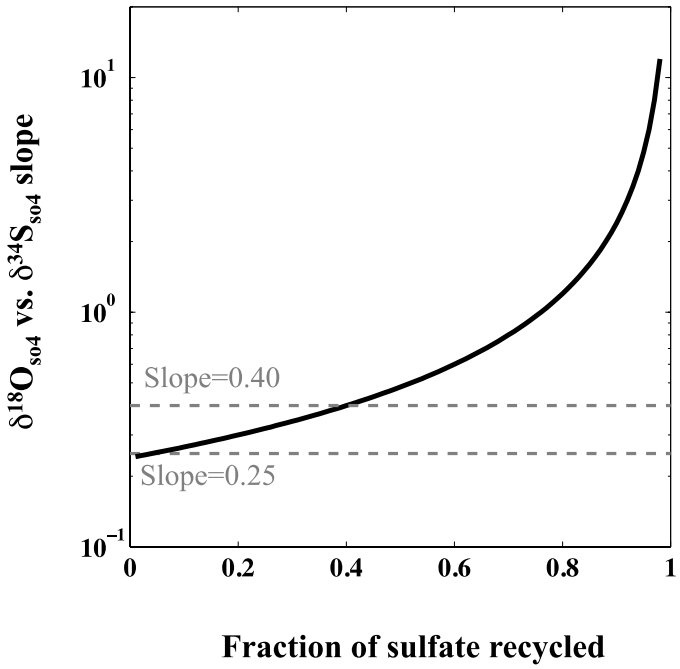

Figure DR.6: The change in the slope of $\delta^{18}O_{SO4}$ vs. $\delta^{34}S_{SO4}$ as a function of the fraction of sulfate recycled.

Table DR2: Worldwide pore fluid $\delta^{18}O_{SO4}$ vs. $\delta^{34}S_{SO4}$ slope and the coresponding references.

Site name	Location	Type	Slope	Error (2σ)	n[a]	Reference
NA 8[b]	SE Mediterranean Sea	MiE[f]	0.45	0.06	5	Rubin-Blum et al. (2014)
NA 80[c]	SE Mediterranean Sea	MiE[f]	0.34	0.06	12	Rubin-Blum et al. (2014)
2639-3	Gulf of Mexico	MiE[f]	0.34	0.15	5	Aharon and Fu. (2003)
2639-4	Gulf of Mexico	MiE[f]	0.29	0.04	5	Aharon and Fu. (2003)
2647-3	Gulf of Mexico	MiE[f]	0.34	0.16	5	Aharon and Fu. (2003)
Oil	Gulf of Mexico	MiE[f]	0.34	0.06	13	Aharon and Fu. (2000)
Gas	Gulf of Mexico	MiE[f]	0.28	0.04	12	Aharon and Fu. (2000)
Ref	Gulf of Mexico	MiE[f]	0.66	0.3	6	Aharon and Fu. (2000)
Strander Bucht, Station 6	Baltic Sea	MiE[f]	0.45	0.04	10	Strauss et al., (2012)
Strander Bucht, Station 5	Baltic Sea	MiE[f]	0.29	0.13	7	Strauss et al., (2012)
Y1[d]	Yarqon estuary (Israel)	MiE[f]	0.35	0.01	11	Antler et al. (2013)
Y2	Yarqon estuary (Israel)	MiE[f]	0.47	0.05	6	Antler et al. (2013)
Y3	Yarqon estuary (Israel)	MiE[f]	0.37	0.03	8	Antler et al. (2014)
Q2	Qishon estuary (Israel)	MD[g]	0.73	0.16	6	Antler et al. (2014)
OS00-17	Amzon delta	N.D[h]	0.3	0.2	4	Aller et al. (2010)
OS00-16	Amzon delta	N.D[h]	0.29	0.05	6	Aller et al. (2010)
OST-2- LOW	Amzon delta	MD[g]	1.04	0.42	10	Aller et al. (2010)
OST-2- RISING	Amzon delta	MD[g]	0.58	0.12	9	Aller et al. (2010)
PC6[e]	SE Mediterranean Sea	MDL[i]	1.25	0.2	6	This study
BA1	SE Mediterranean Sea	MD[g]	1.06	0.11	8	Antler et al. (2013)
HU	SE Mediterranean Sea	MD[g]	0.99	0.13	5	Antler et al. (2013)
ODP 1082	SW Pacific	MDL[i]	2.2	3.31	4	Turchyn et al. (2006)
ODP 1086	SW Pacific	MD[g]	10.73	7.01	3	Turchyn et al. (2006)
OPD 1225	Peru Margin	MD[g]	4.53	1.37	9	Böttcher et al. (2006); Black et al. (2006)
ODP 1226	Peru Margin	MD[g]	0.96	0.47	4	Böttcher et al. (2006); Black et al. (2006)
ODP 1123	West Africa	MD[g]	1.4	0.24	5	Turchyn et al. (2006)
ODP 1052	NW Atlantic	MD[g]	1.69	0.18	8	Antler et al. (2013)

[a] The number of analyses that were used for the linear regression.

[b] 'Black patch' in figure 1a.

[c] 'Gas seeps' in figure 1a.

[d] 'Estuary' in figure 1a.

[e] 'SMTZ' in figure 1a.

[f] MiE- methane-in-excess

[g] MD- methane-devoid

[h] N.D- methane was not measured

[i] MDL- methane-diffusion-limited

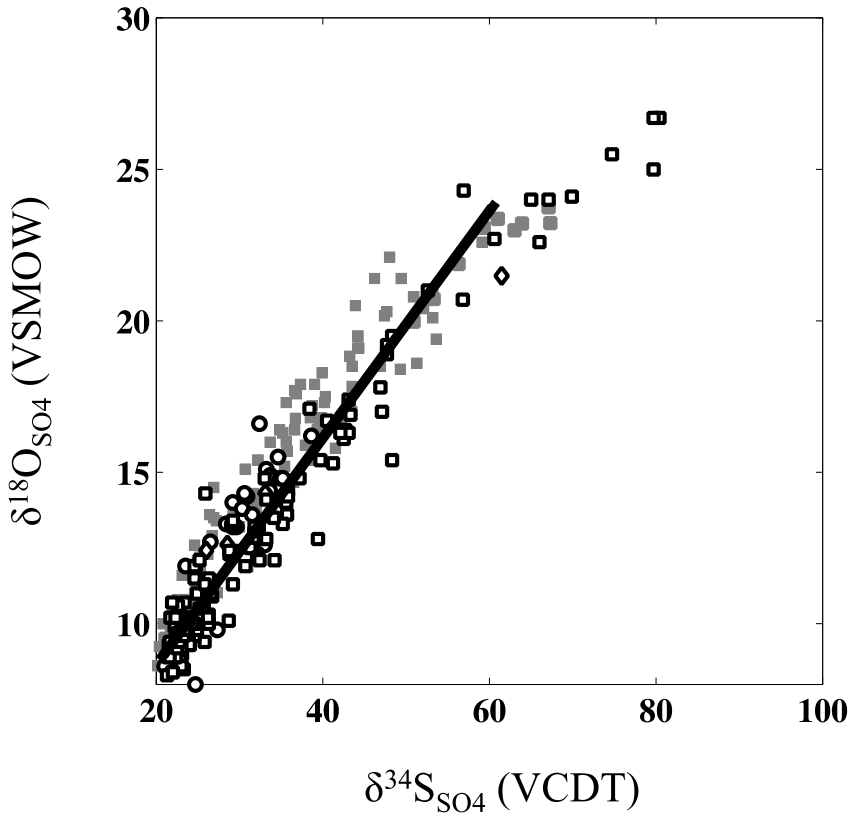

Figure DR.6: The $\delta^{18}O_{SO4}$ vs. $\delta^{34}S_{SO4}$ data from cold methane seeps and seep analogues (grey) and barite deposits associated with cold methane seeps (open symbols) located in the Gulf of Mexico (Rhombus-- Fu and Aharon, 1997, Squares-- Feng and Roberts, 2011) and in the Sea of Okhotsk (Circles-- Greinert et al., 2002). The liner line is the 'methane-in-excess' line from figure 1.

References

Aharon, P. & Fu, B. Microbial sulfate reduction rates and sulfur and oxygen isotope fractionations at oil and gas seeps in deepwater Gulf of Mexico. *Geochim. Cosmochim. Acta*. **64**, 233–246 (2000).

Aharon, P. & Fu, B. Sulfur and oxygen isotopes of coeval sulfate–sulfide in pore fluids of cold seep sediments with sharp redox gradients. *Chem. Geol.* **195**, 201–218 (2003).

Aller, R. C., Madrid, V., Chistoserdov, A., Aller, J. Y., & Heilbrun, C. Unsteady diagenetic processes and sulfur biogeochemistry in tropical deltaic muds: Implications for oceanic isotope cycles and the sedimentary record. *Geochim. Cosmochim. Acta*, **74**, 4671-4692 (2010).

Antler, G., et al. Sulfur and Oxygen Isotope tracing of sulfate driven anaerobic methane oxidation in estuarine sediments. *Est. Coast. Shelf Sci.* **142**, 4-11 (2014).

Antler G., Turchyn, A.V., Rennie, V., Herut, B. & Sivan, O. Coupled sulfur and oxygen isotope insight into bacterial sulfate reduction in the natural environment. *Geochim. Cosmochim. Acta.* **118**, 98–117 (2013).

Blake R. E., Surkov A. V., Böttcher M. E., Ferdelman T. G. and Jørgensen B. B. (2006) Oxygen isotope composition of dissolved sulfate in deep-sea sediments:

Eastern Equatorial Pacific Ocean. Proceedings of the Ocean Drilling Programm, Scientific Results, **201**, 1–24 (2006.

Böttcher M. E., Thamdrup B. and Vennemann T. W. (2001) Oxygen and sulfur isotope fractionation during anaerobic bacterial disproportionation of elemental sulfur. *Geochim. Cosmochim. Acta*,, 65, 1601–1609.

Böttcher, M. E., et al. Sulfur isotope fractionation by the deep biosphere within sediments of the Eastern Equatorial Pacific and Peru Margin. Proceedings of the Ocean Drilling Program, Scientific Results 201, 1–21 (2006).

Milucka, J., et al. Zero-valent sulphur is a key intermediate in marine methane oxidation. *Nature* **491**, 541-546 (2012).

Mizutani, Y. and Rafter, T. A. Oxygen isotopic composition of sulphates – Part 4; bacterial fractionation of oxygen isotopes in the reduction of sulphates and in the oxidation of sulphur. *N. Z. J. Sci*. **12**, 60–68 (1969).

Rees, C. E., A steady-state model for sulphur isotope fractionation in bacterial reduction processes. *Geochimica et Cosmochimica Acta*, v. 37, p. 1141-1162. (1973)

Rubin-Blum, M., et al. Hydrocarbon-related microbial processes in the deep sediments of the Eastern Mediterranean Levantine Basin. *FEMS Microbiol. Ecol.* **87**, 780–796 (2014).

Strauss, H., et al. Sulphur diagenesis in the sediments of the Kiel Bight, SW Baltic Sea, as reflected by multiple stable sulphur isotopes. *Isot. Environ. Health Stud*., **48**, 166-179 (2012).

Turchyn, A. V., Sivan, O. & Schrag, D. Oxygen isotopic composition of sulfate in deep sea pore fluid: evidence for rapid sulfur cycling. *Geobiology*, **4**, 191–201 (2006).